MATERIALS CHEMISTRY
FRONTIERS

RESEARCH ARTICLE

View Article Online
View Journal | View Issue

Cite this: *Mater. Chem. Front.*, 2024, **8**, 3214

$FAPbBr_3$@GA_2PbBr_4 quantum dots: one step fabrication with improved stability for light-emitting applications†

Jiaqi Liu,[a] Feng Zhang, *[b] Cuihe Fan,[a] Zhengwei Cao[a] and Yuying Hao *[a]

Received 28th April 2024,
Accepted 23rd July 2024

DOI: 10.1039/d4qm00354c

rsc.li/frontiers-materials

Perovskite quantum dots (QDs), with outstanding properties, including tunable emissions, high color purity, and low cost solution processability, have become promising candidates in light-emitting applications. However, the inherent instability issue strongly restricts further development and commercialization of light-emitting devices based on perovskite QDs. As well investigated in conventional QDs, the construction of QDs with core–shell structure is recognized as an effective way to improve the stability and optimize luminescent properties at the same time. Inspired by the unique structure diversity of perovskite materials, 2D/3D $FAPbBr_3$@GA_2PbBr_4 QDs are proposed and fabricated through a one-step phase transfer enhanced emulsion synthesis. By systematically tuning the ratio between GABr and FABr as well as a combined analysis with X-ray diffraction, transmission electron microscopy, X-ray photoelectron spectroscopy, absorption and photoluminescence spectrum characterizations, a well-defined core–shell structure is demonstrated for $FAPbBr_3$@GA_2PbBr_4 QDs under an appropriate ratio of GABr/FABr. Compared to the original QDs, the as fabricated core–shell QDs exhibit an enhanced exciton binding energy and improved stability under heat, light, and moisture exposure. Moreover, phosphor converted light-emitting diodes based on the core–shell QDs are also fabricated with a much improved device performance than that of QDs without a core–shell structure, proving the superiority of $FAPbBr_3$@GA_2PbBr_4 QDs in light-emitting applications.

Introduction

Due to their unique properties, such as narrow emission line width, high photoluminescence quantum yields (PLQYs), tunable wavelength covering the entire visible region and low cost solution fabrication process, perovskite quantum dots (QDs) have shown great potential applications in optoelectronic devices including solar cells, light-emitting diodes (LEDs), lasers and photodetectors.[1–4] Especially in LEDs, both perovskite QD based phosphor converted LEDs and electroluminescence (EL) devices have witnessed a rapid development in the past several years.[5–7] For example, phosphor converted LEDs using perovskite QDs as color converters have achieved an ultra-wide color gamut of 140% National Television Standards Committee (NTSC).[8] The external quantum efficiency (EQE) of electroluminescent (EL) devices based on perovskite QDs has experienced a rapid development from 0.76% to exceeding 25%, which is almost comparable to that of organic LEDs or conventional QD based LEDs.[9–13] The excellent performance of perovskite QDs in display devices attracts a broad interest and intense attention from both academic research and industrial development.[14]

Although the applications of perovskite QDs in display technologies have made remarkable achievements, the stability issues of QDs strongly restrict the long-term operation of QD based devices.[15,16] In essence, the ionic nature and low formation energy are the main reasons for the instability of perovskites. To overcome this, numerous encapsulation strategies are explored, including composing with polymers, growing into in organic lattice, and coating with oxide shells.[17–21] What is insufficient is that these strategies only provide a physical barrier to protecting perovskites from oxygen and moisture. Except for the optical properties, the conductivity and solution processibility are strongly affected by the above encapsulation

[a] *Key Laboratory of Advanced Transducers and Intelligent Control System (Ministry of Education), Taiyuan University of Technology, Taiyuan 030024, China. E-mail: haoyuying@tyut.edu.cn*
[b] *School of Physics and Optoelectronic Engineering, Beijing University of Technology, Beijing 100124, China. E-mail: fengzhang@bjut.edu.cn*

† Electronic supplementary information (ESI) available: Analysis of the size distribution of the core–shell QDs, XPS spectra for samples x = 0, x = 0.4 and x = 0.8, plots of FWHM as a function of temperature for $FAPbBr_3$ QDs and $FAPbBr_3$@GA_2PbBr_4 QDs, results of the photostability and moisture stability tests, detailed addition amounts of FABr, GABr, and $PbBr_2$ for fabrication of the core–shell QDs and fitting results of the average PL lifetime. See DOI: https://doi.org/10.1039/d4qm00354c

strategies. Inspired by the research in conventional QDs, the formation of a core–shell structure is demonstrated as an effective way to regulate the optoelectronic properties and enhance the stability of QDs simultaneously.[22–24] Up to now, preliminary progress has been made on the construction of core–shell perovskite QDs, including $CsPbBr_3/SiO_2$ nanoparticles, $CsPbBr_3$/ZnS NCs, $FAPbBr_3/CsPbBr_3$ NCs, *etc.*[25–28] However, these core–shell perovskite QDs reported in the literature still face some shortages, such as poor conductivity (especially for oxide shells, like SiO_2), complex fabrication process (precisely designed technique for shell growth), and an unignored lattice mismatch between the core and shell molecules. Therefore, it is of great significance to explore core–shell perovskite QDs with new components and structures.

Here, based on the structural characteristics of perovskite materials, a new type of core–shell structure, 2D/3D core–shell structured $FAPbBr_3@GA_2PbBr_4$ QDs, was fabricated through a phase transfer enhanced emulsion strategy. The preparation of $FAPbBr_3@GA_2PbBr_4$ QDs can be accomplished in a one-step synthesis due to the selectivity of formamidine (FA) and guanidine (GA) cations in the core and shell. The influence of the GA^+/FA^+ ratio on the formation of $FAPbBr_3@GA_2PbBr_4$ QDs is also studied by varying the amount of GABr in the precursor solution. The optimal ratio of GA^+ leading to the formation of high quality core–shell structured $FAPbBr_3@GA_2PbBr_4$ QDs is demonstrated through a combined analysis with X-ray diffraction (XRD), transmission electron microscopy (TEM), absorption spectra, and steady and time-resolved photoluminescence (PL) spectra. Meaningfully, the as fabricated core–shell $FAPbBr_3@GA_2PbBr_4$ QDs show a greatly enhanced stability under light, heat and moisture compared to original $FAPbBr_3$ QDs. Finally, phosphor converted LED devices are fabricated based on $FAPbBr_3@GA_2PbBr_4$ QDs, proving their superiority in perovskite based optoelectronics.

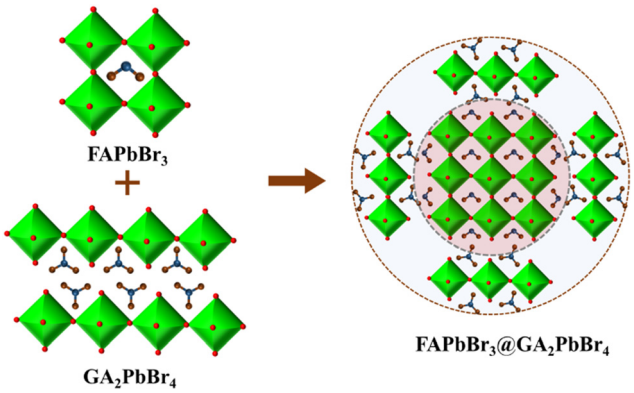

Fig. 1 Schematic illustration of the formation process of 2D/3D core–shell $FAPbBr_3@GA_2PbBr_4$ QDs.

Results and discussion

The formation of perovskite–perovskite heterojunctions utilizing compositional engineering has become a versatile strategy for the fabrication of perovskite QDs with varied optical properties. In our attempt, perovskites with the A site of FA^+ and GA^+ were used for the construction of core–shell perovskite QDs. Due to the limitation of the tolerance factor, GA^+ cations with a larger ionic radius will form a two dimensional (2D) GA_2PbBr_4 structure rather than the 3D structure of the $FAPbBr_3$ constructed by FA^+ cations.[29–31] Therefore, it can be assumed that the addition of GA^+ in a mixed system would not enter the 3D $FAPbBr_3$ core and would exist on the surface of the $FAPbBr_3$ crystal to further induce the formation of GA_2PbBr_4, as shown in Fig. 1. Based on this assumption, 2D/3D core–shell $FAPbBr_3@GA_2PbBr_4$ QDs can be formed in a one pot synthesis, which greatly simplifies the fabrication process of core–shell perovskite QDs.

To verify this, a related synthesis process was conducted based on our previously reported phase transfer enhanced emulsion reprecipitation strategy (detailed fabrication process can be related to the Experiment section).[32–34] As shown in Fig. 2a, firstly, octylamine and oleic acid were added into 1-hexane to assist the foundation of an emulsion system. Then, a fixed amount of FABr, $PbBr_2$, and GABr were dissolved in DMF to form the precursor solution. Under vigorous stirring, the precursor solution was swiftly injected into the mixture of 1-hexane, octylamine and oleic acid. Later, 6 mL of acetonitrile (ACN) were added into the mixture to induce the demulsify process and nucleation of perovskite QDs because of the relatively low saturated concentration of perovskite precursors in ACN. Knowing the fact that ACN is miscible with DMF but immiscible with hexane, the newly formed QDs nucleated in DMF and the ACN phase spontaneously transferred into the hexane phase, greatly avoiding the degradation of QDs by DMF. Finally, solution stratification was accomplished after removing the stirring with QDs dispersed in hexane as the top layer and an ACN/DMF mixture as the bottom layer. The top layer of the QD solution was then collected and purified with ethyl acetate for further characterizations. To explore the addition of

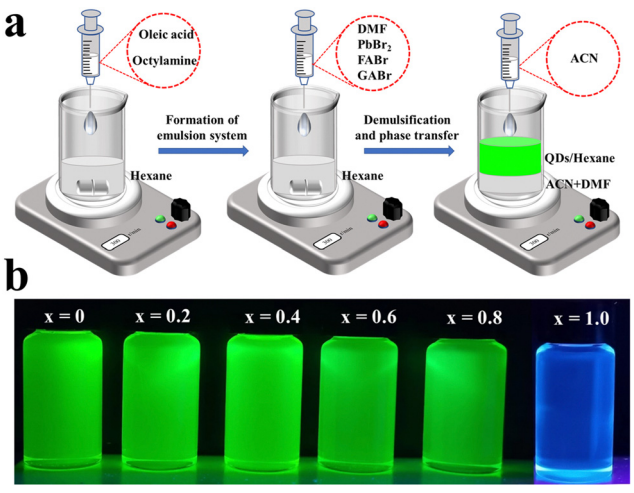

Fig. 2 Fabrication of core–shell QDs. (a) Schematic illustration of the fabrication process of 2D/3D core–shell $FAPbBr_3@GA_2PbBr_4$ QDs. (b) Photographs of the resultant QDs with varied amounts of GABr under UV radiation (365 nm).

GA^+ on the formation of the core–shell structures, the molar ratio between GABr and FABr was adjusted from 0 to 1 with the resulting samples denoted as x = 0, x = 0.2, x = 0.4, x = 0.6, x = 0.8 and x = 1 (detailed addition amounts can be found in Table S1 in ESI†). As shown in Fig. 2b, the as-fabricated QDs dispersed in toluene with the GABr ratio varying from 0 to 0.8 exhibited similar bright green emissions. While QDs with x = 1.0 exhibited a blue emission which most possibly originated from pure GA_2PbBr_4 with a 2D layered structure. To further explore the abrupt color changes from green to blue, the ratio of GABr was finely tuned between 0.8 and 1 with x = 0.85, 0.9 and 0.95. Bluish-green samples were obtained with dual emissions in both the green and blue regions, indicating the occurrence of phase separation rather than formation of a core–shell structure with x larger than 0.8 (see Fig. S1 in ESI†). Moreover, unlike the other samples, QDs with x = 1.0 could not be well dispersed in toluene and precipitated from the solution after storage for 2 h.

TEM and high resolution TEM (HRTEM) characterizations were first applied to acquire the morphology information of the as fabricated perovskite QDs. QDs of x = 1.0 were not characterized due to their poor dispersity. As shown in Fig. 3a–e, QD samples with different amounts of GABr exhibited similar cubic shaped nanoparticles. It can be observed that the particle sizes of the QDs are slightly increased and subsequently decreased with increasing amounts of GABr (see Fig. S2 in ESI†). QDs with a GABr ratio of 0.4 show the most uniform morphology and good dispersity with an average size of 11.8 nm. With increasing the amounts of GABr to 0.6 and 0.8, the boundaries of the as fabricated QDs gradually become indistinct, implying a decreased crystallinity. To further estimate the crystallinity of the as fabricated QDs, HRTEM was applied on typical QDs with a GABr ratio of 0.4. As shown in Fig. 3f, a clear crystal lattice is observed with interplanar distances of 0.29 nm and 0.26 nm corresponding to the (200) and (210) crystal faces of $FAPbBr_3$, respectively. However, crystal faces that originated from GA_2PbBr_4 could not be well identified from the HRTEM image, which might be related to the instability of the GA_2PbBr_4 shell under high energy electron beams.[35]

To further investigate the crystal structure and optical properties of the as fabricated QDs, XRD, X-ray photoelectron spectroscopy (XPS), absorption spectroscopy, and steady and time resolved PL were applied. Fig. 4a shows the XRD patterns of the as fabricated QDs with varied amounts of GABr. QDs with x = 0 show the main diffraction peaks of 15.1° and 30.2°, which are remarkable characteristics of the (100) and (200) crystal faces that originate from the $FAPbBr_3$ perovskite in the cubic phase.[36,37] While QDs with x = 1.0 show a typical 2D layered GA_2PbBr_4 perovskite with diffraction peaks of 8.6°, 9.5°, 12.8°and 17.1°, *etc.*[38–40] With x ranging from 0.2 to 0.8, the two main characteristic peaks of $FAPbBr_3$ located at 15.1° and 30.2° are well maintained in the corresponding XRD patterns, which indicates that the 3D $FAPbBr_3$ structure is dominant in QDs with a GABr content below 0.8. Besides, the obviously widened XRD pattern of x = 0.8 reflects a poor crystallinity with a GA content of 0.8, which is consistent with the unclear crystal grains observed in the TEM image (Fig. 3e). The hardly distinguishable crystal lattice in the HRTEM image (see Fig. S3 in ESI†) confirms the low crystallinity of sample x = 0.8. Except for the two main peaks, it should be noted that additional peaks at 9.6° and 12.8° are also observed in the XRD patterns with x from 0.2 to 0.8 (as indicated by the dashed frame in Fig. 4a). Specifically, an inconspicuous peak at 9.6° appeared in the XRD pattern of x = 0.2, while these two small peaks (9.6° and 12.8°) are simultaneously observed in x = 0.4, x = 0.6 and x = 0.8 (see enlarged XRD pattern in Fig. S4, ESI†), especially for x = 0.4. Through comparing with the XRD pattern of the pure GA_2PbBr_4 perovskite with x = 1.0, it can be found that the observed peaks of 9.6° and 12.8° in QDs with x from 0.2 to 0.8 are consistent with the corresponding peaks of x = 1.0. This implies that the 2D GA_2PbBr_4 structure is also formed in QDs with x from 0.2 to 0.8. To reveal the distribution or connection between $FAPbBr_3$ and GA_2PbBr_4, XPS analysis (Br-3d, Pb-4f, and full spectra) were applied on QDs with x = 0, x = 0.4 and x = 0.8 (see Fig. S5 in ESI†). The Pb-4f

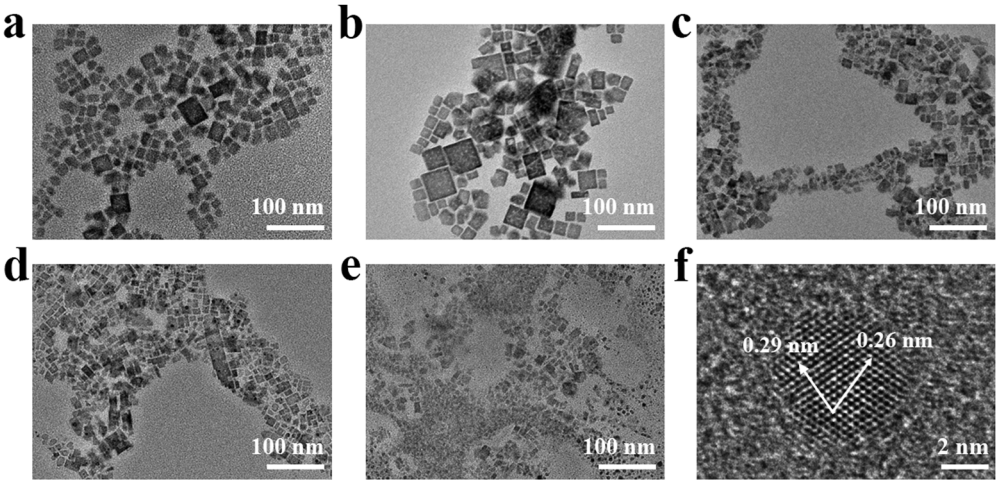

Fig. 3 TEM images of the as fabricated QDs with varied amounts of GABr. x = 0 (a), x = 0.2 (b), x = 0.4 (c), x = 0.6 (d), x = 0.8 (e). (f) HRTEM images of perovskite QDs with a GABr ratio of 0.4.

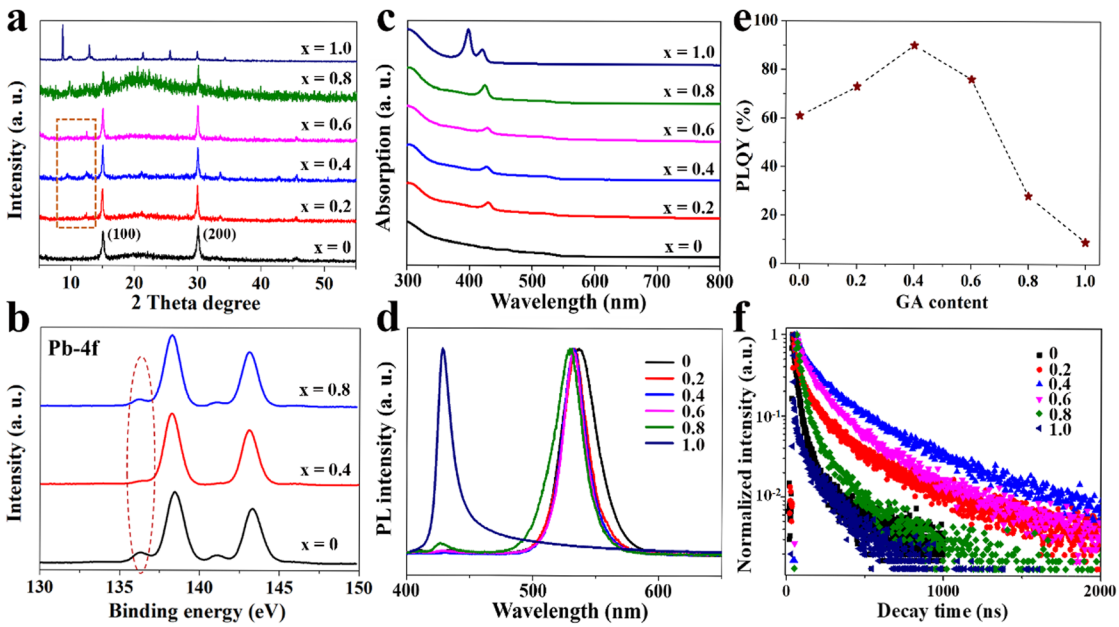

Fig. 4 Structure analysis of the as-fabricated QDs. (a) XRD patterns of typical QD samples with varied amounts of GABr. (b) XPS spectra of QDs with x = 0, x = 0.4 and x = 0.8. Absorption spectra (c), PL spectra (d), PLQY results (e) and time resolved PL spectra of typical QD solutions with x ranging from 0 to 1 (f).

spectra are analyzed in detail as shown in Fig. 4b. All of the QDs exhibit similar XPS spectra with two main peaks of 138.1 eV and 143. 1 eV, which are attributed to Pb-4$f_{5/2}$ and Pb-4$f_{7/2}$.

Besides the main peaks, small shoulder peaks with binding energies of 136.2 eV and 141.3 eV can also be observed for QDs with x = 0 and x = 0.8. These shoulder peaks are considered to be related to Pb defects in the surfaces or interfaces.[41,42] The absence of these shoulder peaks in QDs with x = 0.4 demonstrates the reduced Pb defects, most probably due to the well passivated interfaces between $FAPbBr_3$ and GA_2PbBr_4. Fig. 4c and d show the absorption and PL spectra of the as-fabricated QDs. Pure $FAPbBr_3$ QDs (x = 0) exbibit an absorption band edge at 520 nm while pure GA_2PbBr_4 exhibits absorption peaks at 400 and 417 nm attributed to the layered structure. The absorption spectra of QDs with x = 0.2 to 0.8 simultaneously show the absorption features of $FAPbBr_3$ and GA_2PbBr_4, indicating the coexistence of $FAPbBr_3$ and GA_2PbBr_4. From Fig. 4d, QDs with x = 0 to 0.8 show similar PL spectra, with emission peaks gradually blue shifted from 534 nm to 529 nm while an emission peak of 426 nm is observed for pure GA_2PbBr_4 with x = 1.0. It should be noted that a small PL peak at 426 nm can also be observed for QDs with x = 0.8, indicating a slight phase separation of GA_2PbBr_4 and $FAPbBr_3$. For QDs with x from 0.2 to 0.6, the simultaneously observed absorption features from 2D GA_2PbBr_4 and 3D $FAPbBr_3$ as well as the single PL peak originating from 3D $FAPbBr_3$ indicate a strong energy transfer from 2D GA_2PbBr_4 to 3D $FAPbBr_3$, which also implying the formation of core–shell structure. In fact, the energy transfer from the 2D to 3D perovskites has been intensively investigated and widely recognized as an energy funneling effect.[43,44] Besides, the absolute PLQYs of these QDs were determined by an integrated sphere excited at 405 nm with 61%, 76%, 93%, 79%, 23% and 6% for x = 0 to x = 1.0, respectively (Fig. 4e). To better compare the luminescent properties of the resultant QDs, key photophysical parameters, including emission peaks, full wavelength at half maximum (FWHM), PLQYs and chromaticity coordinates in CIE-1931, are summarized in Table 1. These differences in PLQYs are further analyzed through time resolved PL spectra. As shown in Fig. 4f, the PL decay curve can be fitted to (eqn 1) and the average PL lifetimes are calculated by (eqn (2))

$$I = A_1 \exp\left(\frac{-t}{\tau_1}\right) + A_2 \exp\left(\frac{-t}{\tau_2}\right) \quad (1)$$

$$\tau_{av} = \frac{A_1\tau_1 + A_2\tau_2}{A_1 + A_2} \quad (2)$$

The fitting results demonstrate that the average PL lifetime first increases and then decreases as x increases, with the most prolonged PL lifetime achieved for QDs with x = 0.4 (detailed fitting results can be found in Table S2 in ESI†). Moreover, QDs in the solid state (typical QD samples were spin cast into thin films on glass substrates) were also tested with similar decay dynamics observed, which further confirmed the carrier recombination dynamics in these QDs (see Fig. S6 in ESI†). The longest PL lifetime of x = 0.4 implies fewer defects and well

Table 1 The key photophysical parameters for samples x = 0, x = 0.2, x = 0.4, x = 0.6, x = 0.8 and x = 1.0

Sample	PL peak (nm)	FWHM (nm)	PLQY (%)	CIE (x, y)
x = 0	534	22	61	(0.22, 0.71)
x = 0.2	533	22	76	(0.22, 0.72)
x = 0.4	532	21	93	(0.21, 0.74)
x = 0.6	531	20	79	(0.21, 0.72)
x = 0.8	529/426	26/11	23	(0.18, 0.70)
x = 1.0	426	11	6	(0.18, 0.10)

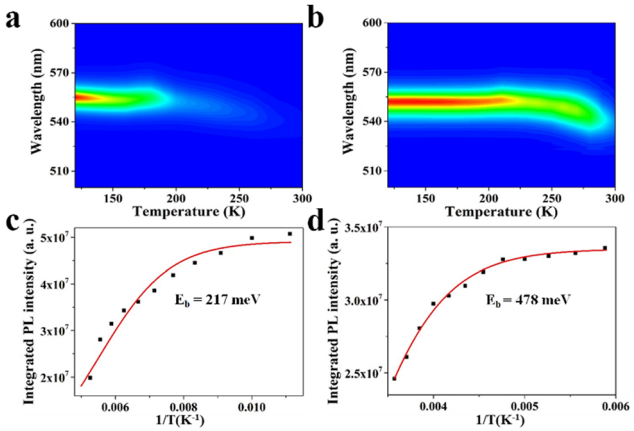

Fig. 5 Pseudo color maps of temperature dependent PL spectra. (a) $FAPbBr_3$ QDs (x = 0). (b) Core–shell $FAPbBr_3$@GA_2PbBr_4 QDs (x = 0.4). (c) and (d) Plots of integrated PL intensity as a function of temperature. $FAPbBr_3$ QDs (x = 0) (c). Core–shell $FAPbBr_3$@GA_2PbBr_4 QDs (x = 0.4) (d).

passivated non-radiative pathways, which is consistent with the XPS and PLQYs results. Based on the above analysis, it can be concluded that the $FAPbBr_3$@GA_2PbBr_4 core shell structure is formed in QDs with x = 0.2 to 0.6 and QDs with x = 0.4 possess a more ideal core–shell structure.

The as fabricated $FAPbBr_3$@GA_2PbBr_4 QDs provide opportunities to explore the influence of the core–shell structure on the luminescent properties of perovskite QDs. Exciton binding energy, acting as an important parameter for semiconductor QDs, was estimated through temperature dependent PL measurements. The corresponding experiment was conducted on an FLS 1000 spectrometer using liquid nitrogen as the cooling medium. The PL intensities of pure $FAPbBr_3$ QDs and $FAPbBr_3$@GA_2PbBr_4 (x = 0.4) QDs were collected from 120 K to 300 K. As shown in Fig. 5a and b, both the $FAPbBr_3$ QDs and $FAPbBr_3$@GA_2PbBr_4 QDs show a decreased PL intensity with temperature increasing. Compared to core–shell $FAPbBr_3$@GA_2PbBr_4 QDs, the PL decline of $FAPbBr_3$ QDs is more rapid. The variation of PL intensity with temperature is plotted in Fig. 5c and d. The related exciton binding energy can be extracted from (eqn (3))

$$I(T) = \frac{I_0}{1 + A\exp\left(-\frac{E_b}{k_B T}\right)} \quad (3)$$

In which $I(T)$ represents the PL intensity at a certain temperature and I_0 represents the PL intensity at 0 K. E_b is the exciton binding energy and k_B is the Boltzmann constant. According to the fitting results, E_b values of 217 meV and 478 meV are obtained for the $FAPbBr_3$ QDs and $FAPbBr_3$@GA_2PbBr_4 QDs, respectively. The relatively 2.2 fold enhanced exciton binding energy indicates that the photogenerated exciton is more stable and exciton recombination occupies a higher proportion in the $FAPbBr_3$@GA_2PbBr_4 QDs, which is consistent with the higher PLQYs of the $FAPbBr_3$@GA_2PbBr_4 QDs.[45] Moreover, along with temperature increasing, the FWHM is also broadening, which can reflect the exciton phonon interactions.[46] The exciton–phonon interaction is calculated through (eqn (4)).

$$\Gamma(T) = \Gamma_0 + \sigma T + \frac{\Gamma_{op}}{\exp(\hbar\omega_{op}/k_B T) - 1} \quad (4)$$

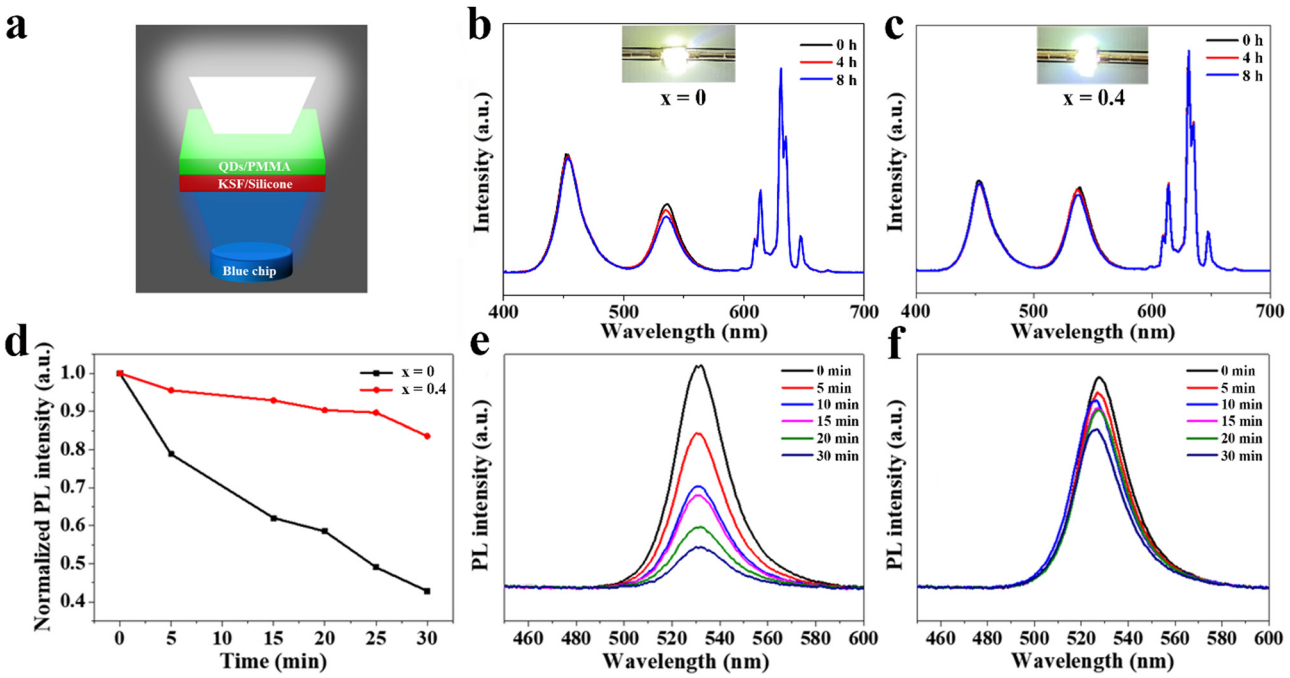

Fig. 6 Potential applications in phosphor converted LED devices. (a) Device structure of phosphor converted LEDs. (b) and (c) The corresponding EL spectra of LED devices based on $FAPbBr_3$ QD and $FAPbBr_3$/GA_2PbBr_4 QD based LED devices, respectively. (d) The variation of PL intensity under heating at 373 K. (e) and (f) The PL spectra of $FAPbBr_3$ QDs and $FAPbBr_3$/GA_2PbBr_4 QDs at 0 min, 5 min, 10 min, 15 min, 20 min and 30 min under 373 K thermal heating.

In eqn 4, the first item Γ_0 is the inhomogeneous broadening contribution. σ and Γ_{op} describe the interactions of exciton acoustic phonon and exciton optical phonon contributions to the line width broadening, respectively. $\hbar\omega_{op}$ describes the optical phonon energy. The fitting results reveal that $FAPbBr_3@GA_2PbBr_4$ QDs possess a larger optical phonon energy (27.7 meV) than that of pure $FAPbBr_3$ QDs (24.1 meV) (The fitting curves can be related to Fig. S7 in ESI†). This enhanced optical phonon interaction may well explain the narrower FWHM and strong anti-broadening effect of $FAPbBr_3@GA_2PbBr_4$ QDs.

Finally, the potential applications of the as fabricated $FAPbBr_3@GA_2PbBr_4$ QDs in wide color gamut displays are explored. Pure $FAPbBr_3$ QDs are also applied for comparison. As shown in Fig. 6a, the as-fabricated QDs are incorporated in PMMA to form a QD/PMMA composite film. A thin layer of the QD/PMMA composite film is deposited on a blue LED chip as a green emitter. Meanwhile, Mn^{2+}:K_2SiF_6 (KSF) powder mixed with silica gel is also introduced to generate white light. Fig. 6b and c show the resulting EL spectra of $FAPbBr_3$ QD and $FAPbBr_3@GA_2PbBr_4$ QD based LED devices, respectively. Both the LED devices based on $FAPbBr_3$ QDs and $FAPbBr_3@GA_2PbBr_4$ QDs emit a bright white light composed of blue (blue LED chip), green (QDs/PMMA) and red (KSF/silica) with CIE coordinates of (0.30, 0.31) and (0.25, 0.26). To evaluate the operation stability, the LED devices were illuminated for 8 h. From Fig. 6b and c, it can be seen that the EL spectra in the green region originated from $FAPbBr_3$ QDs gradually declining after continuous operation. While almost no significant changes in the green region are observed from the EL spectra of $FAPbBr_3@GA_2PbBr_4$ QD based LED devices. In order to further demonstrate the enhanced stability of $FAPbBr_3@GA_2PbBr_4$ QDs, the PL variations of core–shell $FAPbBr_3@GA_2PbBr_4$ QDs and uncoated $FAPbBr_3$ QDs under heat, light radiation and moisture are systematically compared. Fig. 6d shows the variation of PL intensity under thermal heating at 373 K. Fig. 6e and f are the corresponding PL spectra of $FAPbBr_3$ QDs and $FAPbBr_3@GA_2PbBr_4$ QDs detected at different heating periods. It can be seen that the PL intensity of the $FAPbBr_3$ QDs experiences a rapid decreasing and only 40% of the initial PL is maintained. While the PL intensity of $FAPbBr_3@GA_2PbBr_4$ QDs is slightly decreased and over 85% of the initial intensity is preserved after heating for 30 min. Besides, compared to the severely declined PL of $FAPbBr_3$ QDs, over 70% of the initial PL is maintained after light radiation for 30 h and nearly 83% of the initial PL is maintained after moisture treatment for 100 min, as for $FAPbBr_3@GA_2PbBr_4$ QDs (see Fig. S8 in ESI†). The greatly enhanced stability of core–shell $FAPbBr_3@GA_2PbBr_4$ QDs can be attributed to the protection of the 2D GA_2PbBr_4 shell, which makes them more promising candidate in LED applications.

Conclusions

In summary, starting from the structural features of perovskite crystals, a new type of core–shell structure, 2D/3D $FAPbBr_3@GA_2PbBr_4$ QDs, was proposed and fabricated through a phase transfer enhanced emulsion strategy. Because of the self selectivity of the FA^+ and GA^+ cations in the core–shell structure, the fabrication of $FAPbBr_3@GA_2PbBr_4$ QDs can be accomplished in a one pot synthesis without a complicated regulation process. By systematically varying the addition amount of GABr, the construction mechanism of the core–shell structure was clarified. Well-defined 2D/3D $FAPbBr_3@GA_2PbBr_4$ QDs with maximum PLQYs up to 93% were obtained under an optimized ratio of GABr. The influence of the core–shell structure on the luminescent properties was intensively studied through absorption spectra, steady and time-resolved PL as well as temperature dependent spectroscopy. Fewer defect states and a 2.2 fold enhanced exciton binding energy compared to pure that of $FAPbBr_3$ QDs were revealed, which well explained the improved luminescent properties of $FAPbBr_3@GA_2PbBr_4$ QDs. Moreover, the as fabricated core–shell $FAPbBr_3@GA_2PbBr_4$ QDs exhibited a greatly enhanced stability under light, heat and moisture compared to that of the uncoated $FAPbBr_3$ QDs. The superiority of $FAPbBr_3@GA_2PbBr_4$ QDs in LED devices was demonstrated with a much prolonged operation lifetime, proving their promising prospect in lighting and display technologies.

Experimental section

Materials

All the reagents were used as received without further purification. $PbBr_2$ (lead(II) bromide 99%, Aladdin), formamidine bromide (FABr, 99.5%, Xi'an Yuri Solar Co., Ltd), guanidine bromide (GABr, Xi'an Yuri Solar Co., Ltd), *n*-octylamine (99%, Aladdin), oleic acid (OA, 90%, Alfa Aesar), *N*,*N*-Dimethylformamide (DMF, analytical grade, Beijing Chemical Reagent Co., Ltd, China), acetonitrile (ACN, analytical grade, Beijing Chemical Reagent Co., Ltd, China), toluene (analytical grade, Beijing Chemical Reagent Co., Ltd, China), ethyl acetate (analytical grade, Beijing Chemical Reagent Co., Ltd, China), K_2SiF_6:Mn^{4+} (KSF, Beijing Yuji Science & Technology Co., Ltd, China), and poly(methyl methacrylate) (PMMA, average MW ~35 000, Alfa Aesar).

Preparation of $FAPbBr_3/GA_2PbBr_4$ QDs

Colloidal $FAPbBr_3/GA_2PbBr_4$ QDs were fabricated through modifications of the phase transfer enhanced emulsion reprecipitation strategy. For pure $FAPbBr_3$ QDs, 0.2 mmol FABr and 0.2 mmol $PbBr_2$ were dissolved in 1 mL of DMF to form a precursor solution. Before injection of the precursor solution, 15 μL of octylamine and 200 μL of OA were added into 10 mL of hexane to help the formation of the emulsion. Then, with a monitor of the UV light radiation (365 nm), 500 μL of the precursor solution was slowly dropwise added into hexane under vigorous stirring. Then 6 mL of ACN, acting as a demulsifier, was slowly injected into the emulsion system. After the addition of ACN, the mixture spontaneously separated into two layers. After removing the stirring, the top layer was carefully collected as a crude solution. The crude solution was further purified twice by ethyl acetate and redispersed in toluene. For the -shell $FAPbBr_3/GA_2PbBr_4$ QDs, a portion of

FABr was replaced by GABr. The molar ratio between FABr and GABr was systematically adjusted from 10 : 0, 8 : 2, 6 : 4, 4 : 6, 2 : 8 to 0 : 10 to investigate the influence of GABr on the formation of the core–shell structure.

Fabrication of LED devices

A certain amount of PMMA powder was dissolved in toluene after continuous stirring for 24 h to form a PMMA/toluene solution with a fraction of 10% wt. Then, 2 mL of QDs in toluene was mixed with 1 mL of the PMMA/toluene solution and drop cast into QD/PMMA composite films after evaporation of the toluene. KSF powder (0.5 g) was blended with an equivalent (1 g) of silicone gel A and B followed by waiting for 30 min to form a KSF/silicone layer. Then, the KSF/silicone layer and $FAPbBr_3$ QD/PMMA composite film were successively painted on the surface of a blue chip for further measurements.

Characterizations

The XRD data were collected on a Bruker/D8 FOCUS X-ray diffractometer. TEM images were captured on a JEOL-JEM 2100F system operating at 200 kV. UV-vis absorption spectra of the QDs were measured using a Shimadzu UV-2600. A fluorescence spectrometer (FLS980, Edinburgh Instruments, E I) was used to measure the steady-state PL and TRPL spectra. XPS spectra were detected using X-ray photoelectron spectroscopy (Thermo Scientific ESCALAB250Xi). Temperature-dependent PL spectra were performed on a fluorescence spectrometer (FLS980, Edinburgh Instruments, E I) equipped with a liquid nitrogen cooler. The absolute PLQYs of the QDs were determined using an integrated sphere (C9920-02, Hamamatsu Photonics, Japan) excited at a wavelength of 450 nm.

Author contributions

The manuscript was written through contributions of all the authors. All the authors have given approval to the final version of the manuscript.

Data availability

The data supporting this article have been included as part of the ESI.†

Conflicts of interest

The authors declare no competing financial interest.

Acknowledgements

This study was supported by the National Natural Science Foundation of China (52303219), Beijing Postdoctoral Research Foundation (2023-zz-53), NSFC-Joint Foundation Program for Regional Innovation and Development (U21A20102), Major Special Projects of Shanxi Province in Science and Technology (202202060301003), and Fundamental Research Program of Shanxi Province (20210302124391).

Notes and references

1 T. Chiba and J. Kido, Lead halide perovskite quantum dots for light-emitting devices, *J. Mater. Chem. C*, 2018, **6**, 11868–11877.
2 C. Bi, S. V. Kershaw, A. L. Rogach and J. Tian, Improved stability and photodetector performance of $CsPbI_3$ perovskite quantum dots by ligand exchange with aminoethanethiol, *Adv. Funct. Mater.*, 2019, **29**, 1902446.
3 M. Hao, S. Ding, S. Gaznaghi, H. Cheng and L. Wang, Perovskite Quantum Dot Solar Cells: Current Status and Future Outlook, *ACS Energy Lett.*, 2024, **9**, 308–322.
4 H. Zhu, S. Teale, M. N. Lintangpradipto, S. Mahesh, B. Chen, M. D. McGehee, E. H. Sargent and O. M. Bakr, Long-term operating stability in perovskite photovoltaics, *Nat. Rev. Mater.*, 2023, **8**, 569–586.
5 K. B. Lin, J. Xing, L. N. Quan, F. P. G. deArquer, X. W. Gong, J. Lu, L. Xie, W. Zhao, D. Zhang, C. Yan, W. Li, X. Liu, Y. Lu, J. Kirman, E. H. Sargent, Q. Xiong and Z. Wei, Perovskite Light-Emitting Diodes with External Quantum Efficiency Exceeding 20 Percent, *Nature*, 2018, **562**, 245–248.
6 J. S. Kim, J. M. Heo, G. S. Park, S. J. Woo, C. Cho, H. J. Yun, D. H. Kim, J. Park, S. C. Lee, S. H. Park, E. Yoon, N. C. Greenham and T. W. Lee, Ultra-Bright, Efficient and Stable Perovskite Light-Emitting Diodes, *Nature*, 2022, **611**, 688–694.
7 G. H. Lee, K. Kim, Y. Kim, J. Yang and M. K. Choi, Recent Advances in Patterning Strategies for Full-Color Perovskite Light-Emitting Diodes, *Nano-Micro Lett.*, 2024, **16**, 39.
8 L. Protesescu, S. Yakunin, M. I. Bodnarchuk, F. Krieg, R. Caputo, C. H. Hendon, R. X. Yang, A. Walsh and M. V. Kovalenko, Nanocrystals of Cesium Lead Halide Perovskites ($CsPbX_3$, X = Cl, Br, and I): Novel Optoelectronic Materials Showing Bright Emission with Wide Color Gamut, *Nano Lett.*, 2015, **15**, 3692–3696.
9 Z. K. Tan, R. S. Moghaddam, M. L. Lai, P. Docampo, R. Higler, F. Deschler, M. Price, A. Sadhanala, L. M. Pazos, D. Credgington, F. Hanusch, T. Bein, H. J. Snaith and R. H. Friend, Bright Light-Emitting Diodes based on Organometal Halide Perovskite, *Nat. Nanotechnol.*, 2014, **9**, 687–692.
10 D. Ma, K. Lin, Y. Dong, H. Choubisa, A. H. Proppe, D. Wu, Y. K. Wang, B. Chen, P. Li, J. Z. Fan, F. Yuan, A. Johnston, Y. Liu, Y. Kang, Z. H. Lu, Z. Wei and E. H. Sargent, Distribution Control Enables Efficient Reduced-Dimensional Perovskite LEDs, *Nature*, 2021, **599**, 594–598.
11 H. Cho, S. H. Jeong, M. H. Park, Y. H. Kim, C. Wolf, C. L. Lee, J. H. Heo, A. Sadhanala, N. Myoung, S. Yoo, S. H. Im, R. H. Friend and T. W. Lee, Overcoming the Electroluminescence Efficiency Limitations of Perovskite Light-Emitting Diodes, *Science*, 2015, **350**, 1222–1225.
12 W. Xu, Q. Hu, S. Bai, C. Bao, Y. Miao, Z. Yuan, T. Borzda, A. J. Barker, E. Tyukalova, Z. Hu, M. Kawecki, H. Wang, Z. Yan, X. Liu, X. Shi, K. Uvdal, M. Fahlman, W. Zhang, M. Duchamp, J. M. Liu, A. Petrozza, J. Wang, L. M. Liu, W. Huang and F. Gao, Rational Molecular Passivation for

High-Performance Perovskite Light-Emitting Diodes, *Nat. Photonics*, 2019, **13**, 418–424.
13 Y. Cao, N. Wang, H. Tian, J. Guo, Y. Wei, H. Chen, Y. Miao, W. Zou, K. Pan, Y. He, H. Cao, Y. Ke, M. Xu, Y. Wang, M. Yang, K. Du, Z. Fu, D. Kong, D. Dai, Y. Jin, G. Li, H. Li, Q. Peng, J. Wang and W. Huang, Perovskite Light-emitting Diodes based on Spontaneously Formed Submicrometre Scale Structures, *Nature*, 2018, **562**, 249–253.
14 X. G. Wu, H. L. Ji, X. L. Yan and H. Z. Zhong, Industry Outlook of Perovskite Quantum Dots for Display Applications, *Nat. Nanotechnol.*, 2022, **17**, 813–816.
15 C. Zhang, J. Chen, L. Kong, L. Wang, S. Wang, W. Chen, R. Mao, L. Turyanska, G. Jia and X. Yang, Core/Shell Metal Halide Perovskite Nanocrystals for Optoelectronic Applications, *Adv. Funct. Mater.*, 2021, **31**, 2100438.
16 Z. Cao, F. Zhang, J. Liu, C. Fan, Y. Wu and Y. Hao, Recent Advances in Encapsulation of Highly Stable Perovskite Nanocrystals and their Potential Applications in Optoelectronic Devices, *Phys. Chem. Chem. Phys.*, 2023, **25**, 17725–17736.
17 Z. Wang, R. Fu, F. Li, H. Xie, P. He, Q. Sha, Z. Tang, N. Wang and H. Zhong, One-Step Polymeric Melt Encapsulation Method to Prepare $CsPbBr_3$ Perovskite Quantum Dots/Polymethyl Methacrylate Composite with High Performance, *Adv. Funct. Mater.*, 2021, **31**, 2010009.
18 Q. Zhang, B. Wang, W. Zheng, L. Kong, Q. Wan, C. Zhang, Z. Li, X. Cao, M. Liu and L. Li, Ceramic-Like Stable $CsPbBr_3$ Nanocrystals Encapsulated in Silica Derived from Molecular Sieve Templates, *Nat. Commun.*, 2020, **11**, 31.
19 W. Yang, F. Gao, Y. Qiu, W. Liu, H. Xu, L. Yang and Y. Liu, $CsPbBr_3$ Quantum-Dots/Polystyrene@Silica Hybrid Microsphere Structures with Significantly Improved Stability for White LEDs, *Adv. Opt. Mater.*, 2019, **7**, 1900546.
20 Y. Wang, J. He, H. Chen, J. Chen, R. Zhu, P. Ma, A. Towers, Y. Lin, A. J. Gesquiere, S. T. Wu and Y. Dong, Ultrastable, Highly Luminescent Organic–Inorganic Perovskite-Polymer Composite Films, *Adv. Mater.*, 2016, **28**, 10710–10717.
21 W. Lv, L. Li, M. Xu, J. Hong, X. Tang, L. Xu, Y. Wu, R. Zhu, R. Chen and W. Huang, Improving the Stability of Metal Halide Perovskite Quantum Dots by Encapsulation, *Adv. Mater.*, 2019, **31**, 1900682.
22 H. Moon, C. Lee, W. Lee, J. Kim and H. Chae, Stability of Quantum Dots, Quantum Dot Films, and Quantum Dot Light-Emitting Diodes for Display Applications, *Adv. Mater.*, 2019, **31**, 1804294.
23 T. J. Kim, S. Lee, E. Lee, C. Seo, J. Kim and J. Joo, Far-Red Interlayer Excitons of Perovskite/Quantum-Dot Heterostructures, *Adv. Sci.*, 2023, **10**, 2207653.
24 H. Shen, Q. Gao, Y. Zhang, Y. Lin, Q. Lin, Z. Li, L. Chen, Z. Zeng, X. Li, Y. Jia, S. Wang, Z. Du, L. S. Li and Z. Zhang, Visible Quantum Dot Light-Emitting Diodes with Simultaneous High Brightness and Efficiency, *Nat. Photonics*, 2019, **13**, 192–197.
25 Z. Hu, Z. Liu, Y. Bian, S. Li, X. Tang, J. Du, Z. Zang, M. Zhou, W. Hu, Y. Tian and Y. Leng, Enhanced Two-Photon-Pumped Emission from *In Situ* Synthesized Nonblinking $CsPbBr_3$/SiO_2 Nanocrystals with Excellent Stability, *Adv. Opt. Mater.*, 2018, **6**, 1700997.
26 Q. X. Zhong, M. H. Cao, H. C. Hu, D. Yang, M. Chen, P. L. Li, L. Z. Wu and Q. Zhang, One-Pot Synthesis of Highly Stable $CsPbBr_3$@SiO_2 Core–Shell Nanoparticles, *ACS Nano*, 2018, **12**, 8579–8587.
27 V. K. Ravi, S. Saikia, S. Yadav, V. V. Nawale and A. Nag, $CsPbBr_3$/ZnS Core/Shell Type Nanocrystals for Enhancing Luminescence Lifetime and Water Stability, *ACS Energy Lett.*, 2020, **5**, 1794–1796.
28 C. Zhang, S. Wang, X. Li, M. Yuan, L. Turyanska and X. Yang, Core/Shell Perovskite Nanocrystals: Synthesis of Highly Efficient and Environmentally Stable $FAPbBr_3$/$CsPbBr_3$ for LED Applications, *Adv. Funct. Mater.*, 2020, **30**, 1910582.
29 D. L. McGott, C. P. Muzzillo, C. L. Perkins, J. J. Berry, K. Zhu, J. N. Duenow, E. Colegrove, C. A. Wolden and M. O. Reese, 3D/2D Passivation as a Secret to Success for Polycrystalline Thin-Film Solar Cells, *Joule*, 2021, **5**, 1057–1073.
30 Z. Li, M. Yang, J. S. Park, S. H. Wei, J. J. Berry and K. Zhu, Stabilizing Perovskite Structures by Tuning Tolerance Factor: Formation of Formamidinium and Cesium Lead Iodide Solid-State Alloys, *Chem. Mater.*, 2016, **28**, 284–292.
31 Y. L. Zhang, P. J. Wang, M. C. Tang, D. Barrit, W. J. Ke, J. X. Liu, T. Luo, Y. C. Liu, T. Q. Niu, D. M. Smilgies, Z. Yang, Z. Liu, S. Jin, M. G. Kanatzidis, A. Amassian, S. F. Liu and K. Zhao, Dynamical Transformation of Two-Dimensional Perovskites with Alternating Cations in the Interlayer Space for High-Performance Photovoltaics, *J. Am. Chem. Soc.*, 2019, **141**, 2684–2694.
32 F. Zhang, H. Zhong, C. Chen, X. Wu, X. Hu, H. Huang, J. Han, B. Zou and Y. Dong, Brightly Luminescent and Color-Tunable Colloidal $CH_3NH_3PbX_3$ (X = Br, I, Cl) Quantum Dots: Potential Alternatives for Display Technology, *ACS Nano*, 2015, **9**, 4533–4542.
33 F. Zhang, C. T. Xiao, Y. F. Li, X. Zhang, J. L. Tang, S. Chang, Q. B. Pei and H. Z. Zhong, Gram-Scale Synthesis of Blue-Emitting $CH_3NH_3PbBr_3$ Quantum Dots Through Phase Transfer Strategy, *Front. Chem.*, 2018, **6**, 8.
34 H. Huang, F. Zhao, L. Liu, F. Zhang, X. Wu, L. Shi, B. Zou, Q. Pei and H. Zhong, Emulsion Synthesis of Size-Tunable $CH_3NH_3PbBr_3$ Quantum Dots: An Alternative Route toward Efficient Light-Emitting Diodes, *ACS Appl. Mater. Interfaces*, 2015, **7**, 28128–28133.
35 C. Ye, J. Jiang, S. Zou, W. Mi and Y. Xiao, Core–Shell Three-Dimensional Perovskite Nanocrystals with Chiral-Induced Spin Selectivity for Room-Temperature Spin Light-Emitting Diodes, *J. Am. Chem. Soc.*, 2022, **144**, 9707–9714.
36 H. Zheng, H. Xu, F. Zheng, G. Liu, X. Xu, S. Xu, L. Zhang and X. Pan, The Effect of Constituent Ratios and Varisized Ammonium Salts on the Performance of Two-Dimensional Perovskite Materials, *ChemSusChem*, 2020, **13**, 252–259.
37 W. C. Xiang and W. Tress, Review on Recent Progress of All-Inorganic Metal Halide Perovskites and Solar Cells, *Adv. Mater.*, 2019, **31**, 28.
38 E. Shi, Y. Gao, B. P. Akriti, A. H. Coffey and L. Dou, Two-Dimensional Halide Perovskite Nanomaterials and Heterostructures, *Chem. Soc. Rev.*, 2018, **47**, 6046–6072.

39 L. L. Mao, C. C. Stoumpos and M. G. Kanatzidis, Two-Dimensional Hybrid Halide Perovskites: Principles and Promises, *J. Am. Chem. Soc.*, 2019, **141**, 1171–1190.
40 F. Zhang, H. P. Lu, J. H. Tong, J. J. Berry, M. C. Beard and K. Zhu, Advances in Two-Dimensional Organic–Inorganic Hybrid Perovskites, *Energy Environ. Sci.*, 2020, **13**, 1154–1186.
41 Z. Xiao, Z. Song and Y. Yan, From Lead Halide Perovskites to Lead-Free Metal Halide Perovskites and Perovskite Derivatives, *Adv. Mater.*, 2019, **31**, 1803792.
42 M. L. Agiorgousis, Y. Y. Sun, H. Zeng and S. Zhang, Strong Covalency-Induced Recombination Centers in Perovskite Solar Cell Material $CH_3NH_3PbI_3$, *J. Am. Chem. Soc.*, 2014, **136**, 14570–14575.
43 M. Yuan, L. N. Quan, R. Comin, G. Walters, R. Sabatini, O. Voznyy, S. Hoogland, Y. Zhao, E. M. Beauregard, P. Kanjanaboos, Z. Lu, D. H. Kim and E. H. Sargent, Perovskite energy funnels for efficient light-emitting diodes, *Nat. Nanotechnol.*, 2016, **11**, 872–877.
44 L. Lei, D. Seyitliyev, S. Stuard, J. Mendes, Q. Dong, X. Fu, Y. A. Chen, S. He, X. Yi, L. Zhu, C. H. Chang, H. Ade, K. Gundogdu and F. So, Efficient energy funneling in quasi-2D perovskites: from light emission to lasing, *Adv. Mater.*, 2020, **32**, 1906571.
45 B. T. Diroll and C. B. Murray, High-Temperature Photoluminescence of CdSe/CdS Core/Shell Nanoheterostructures, *ACS Nano*, 2014, **8**, 6466–6474.
46 C. Quarti, G. Grancini, E. Mosconi, P. Bruno, J. M. Ball, M. M. Lee, H. J. Snaith, A. Petrozza and F. D. Angelis, The Raman Spectrum of the $CH_3NH_3PbI_3$ Hybrid Perovskite: Interplay of Theory and Experiment, *J. Phys. Chem. Lett.*, 2014, **5**, 279–284.

